Sensitivity of Drivetrain Condition Monitoring Signals to Wind Turbine Blade Damage

Watson, Simon J.; Pal, Sumit K.; Zappalá, Donatella; Nejad, Amir R.

DOI
10.1088/1742-6596/3025/1/012012

Publication date
2025

Document Version
Final published version

Published in
Journal of Physics: Conference Series

PAPER • **OPEN ACCESS**

Sensitivity of Drivetrain Condition Monitoring Signals to Wind Turbine Blade Damage

To cite this article: Simon J Watson *et al* 2025 *J. Phys.: Conf. Ser.* **3025** 012012

Sensitivity of Drivetrain Condition Monitoring Signals to Wind Turbine Blade Damage

Simon J Watson[1*], Sumit K Pal[1], Donatella Zappalá[1] and Amir R Nejad[2]

[1] Faculty of Aerospace Engineering, TUD, Kluyverweg 1, 2629HS, Delft, NL
[2] IMT, NTNU, Jonsvannsveien 82, 7050 Trondheim, Norway

[*]E-mail: S.J.Watson@tudelft.nl

Abstract. This paper studies the sensitivity of drivetrain condition monitoring system (CMS) signals to blade damage, exploring how these signals, particularly vibration, can serve as a potential tool for detection and tracking damage progression. This is achieved using a decoupled simulation approach, combining an aeroelastic solver with a drivetrain model. First, aeroelastic simulations are performed in OpenFAST, where the low-speed shaft (LSS) forces, moments, and tower top position vector are extracted and transferred to the drivetrain model. The drivetrain is modelled using the multi-body simulation environment SIMPACK. Blade damage is introduced in OpenFAST by reducing stiffness in the flap-wise or edgewise direction. The reference DTU-10MW onshore wind turbine is used as a test case. First, the impact of blade damage on LSS shear forces is analysed. Then the drivetrain response is assessed using virtual velocity sensors placed at the main bearing, rear bearing and gearbox housing. Results indicate that damage occurring in the blade mid-span region shows higher sensitivity compared to tip and root locations. A positive correlation is observed between LSS shear force and bearings side-side velocity, with higher forces leading to increased vibration. Additionally, the trend suggests that higher stiffness reduction results in higher velocity, indicating damage progression.

1. Introduction

Wind turbine blades represent a substantial portion of the overall cost of a wind turbine and exhibit a notable failure rate in comparison to other components [1]. Blade failures can reduce turbine yield or, in extreme cases, stop turbine operation and require replacement, which is a time-consuming and costly operation involving heavy lift equipment. Blade monitoring is mainly carried out by visual inspection, either from the ground, using drones, or by physically climbing the blade. Such methods can detect external problems, but not the internal defects. In this study, a preliminary sensitivity analysis of how drivetrain condition monitoring signals respond to blade damage is presented to assess their potential for damage identification. One of the key advantages of using drivetrain CMS signals is that they are commonly available in commercial CMS installed on operational wind turbines, eliminating the need for additional dedicated blade sensors. Leveraging these existing systems for blade damage detection could offer a cost-effective and scalable alternative to more invasive or expensive monitoring solutions, with the potential to detect both internal and external blade damage.

Fremmelev et al. (2023) [2] conducted a full scale wind turbine blade monitoring campaign for the detection of damage initiation and progression due to fatigue-driven loads during in-house testing. They demonstrated that detecting the initiation and progression of damage is possible with an actuator and a single vibration sensor positioned within 10 meters of the damage site. Recently, Varouxis et al. (2024) [3] presented an experimental study to detect fatigue damage propagation in a full scale wind turbine blade. However, deploying an array of accelerometers or strain gauges used by [3] along the entire span of operational wind turbine blades is impractical due to the high costs and additional maintenance requirements . This highlights the need for alternative, cost-effective monitoring solutions.

Popular damage detection methods for operational wind turbine blades include non-destructive testing (NDT) techniques, such as thermography, ultrasonics, acoustic emissions, and vibration analysis [4]. Zhang et al. (2022) [5] investigated the detection of wind turbine blade trailing edge cracks using aerodynamic noise in an experimental setup. Their findings suggest that tonal noise features caused by a cracks can be detected under clean or low turbulent inflow conditions at moderate angles of attack. Khoshmanesh et al. (2022) [6] used infrared thermography to study damage evolution process in the adhesive joint of a representative wind turbine blade section. They highlighted the thermography's advantage in identifying early crack formation and localisation. Although these methods are effective for detecting and localizing damage, they are often costly and time-consuming. Alternatively, leveraging existing drivetrain condition monitoring system (CMS) signals on operational wind turbines, in particular vibration, could serve as a potential practical tool for tracking blade damage progression.

This study presents a preliminary analysis aimed at quantifying the sensitivity of drivetrain CMS signals to blade structural damage. Using the reference DTU-10MW onshore wind turbine as a test case, changes in the RMS value of the first harmonic of the wind turbine rotational frequency (1P) between healthy and damaged blade conditions are analysed to identify potential damage indicators in drivetrain CMS signals. The remainder of this paper is structured as follows: the next section outlines the methodology, followed by a presentation of the results and discussion of the findings, concluding with key insights and future directions.

2. Methodology

This study employs a decoupled simulation approach to analyse the sensitivity of drivetrain condition monitoring signals to blade structural damage. The methodology incorporates:

1. *Aeroelastic Rotor Simulation* – Performed using OpenFAST to compute aeroelastic responses of the wind turbine, including main shaft loads and tower-top motion.
2. *Drivetrain Multi-Body Dynamics Simulation* – Conducted in SIMPACK, using outputs from OpenFAST as inputs to assess drivetrain dynamics and responses.
3. *Coupling* – The interaction between the rotor model in OpenFAST and the drivetrain model in SIMPACK is established to ensure consistent load transfer and dynamic behaviour.
4. *Blade damage model* – Blade structural damage is incorporated into the aeroelastic rotor simulations to assess its impact on system dynamics.
5. *Signal Processing* – The recorded time domain responses are analysed in the frequency domain to extract relevant features for condition monitoring.

2.1 OpenFAST wind turbine model

This paper utilizes OpenFAST [7] to model the coupled dynamics of a wind turbine system. The aerodynamic loads on the blade are computed using the AeroDyn 15 [8] module, which is based

on Blade-Element/Momentum (BEM) theory. The structural dynamics of the tower and blades are modelled using the ElastoDyn module, which requires modal coefficients, damping properties, and elastic parameters for each degree of freedom. The ElastoDyn module allows consideration of only the first two flap wise bending modes and first edge wise bending mode. To model blade damage, the flexural rigidity (EI) in the flap-wise or edge-wise direction is modified at a specific blade location within the ElastoDyn input file. This approach is further discussed in a subsequent section. The Reference Open Source Controller (ROSCO) was used in this setup, which uses collective pitching [9]. The specifications of the DTU 10MW reference wind turbine are listed in Table 1. For this study, a steady state wind condition is considered.

Table 1. Specifications of the DTU 10MW RWT [10]

Parameter	Value
Rating	10 MW
Control	Variable speed, collective pitch, ROSCO
Rotor, Hub diameter (m)	178.3, 5.6
Hub height (m)	119.0
Cut-in, rated, and Cut-out wind speed (m/s)	4, 11.4, and 25
Cut-in, Rated rotor speed (RPM)	6, 9.6
Hub Overhang (m)	7.1
Shaft tilt angle (deg)	5.0
Pre-cone angle (deg)	-2.5
Rotor mass (kg)	227962
Nacelle mass (kg)	446036
Tower mass (kg)	628442

2.2 SIMPACK drivetrain model

Figure 1 shows the layout of the drivetrain model used in this research. A detailed study about this drivetrain model can be found in [11]. The drivetrain has a four-point support and integrates a three-stage gearbox. In the first and second planetary stages, ring gears are fixed to the gearbox housing, which is supported on the bedplate via torque arms. Input torque is applied on the planet carriers, with the sun gears serving as the output torque. In the third parallel stage, torque is transferred from the sun gear of the second planetary stage to the generator through a gear pair (Gear-Pinion) in the high-speed stage. This configuration converts high torque on the low-speed shaft to lower torque on the high-speed shaft. Gear teeth contact is modelled using the FE225 force element in SIMPACK, where the contact force is composed of stiffness, damping, and friction terms. The gears and shafts inside the gearbox are treated as rigid bodies. The specifications of the drivetrain are mentioned in the Table 2.

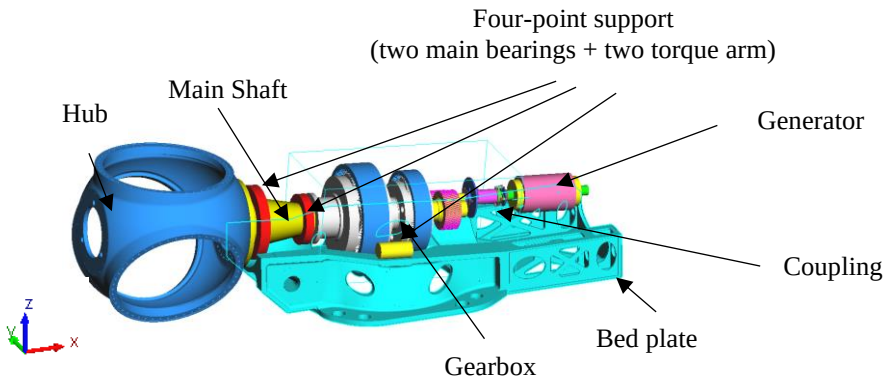

Figure 1. DTU 10MW drivetrain model [11]

Table 2. Drivetrain specifications of DTU 10MW [11]

Parameter	Value
Drivetrain type	Four-point support
Gearbox type	Two planetary + one parallel
First stage ratio	1:4.423
Second stage ratio	1:5.192
Third stage ratio	1:2.179
Total ratio	1:50.039
Rated input shaft speed (rpm)	9.6
Rated generator shaft speed (rpm)	480.4
Rated input shaft torque (kN-m)	9947.9
Rated generator shaft torque (kN-m)	198.8
Gearbox mass (tonne)	60.43
Bedplate mass (tonne)	102.39
Equivalent drive-shaft torsional-spring constant (Nm/rad)	2317025000
Equivalent drive-shaft torsional-damping constant (Nm/(rad/s))	9240560

2.3 Coupling

The coupling between the rotor model, described in Section 2.1, and the drivetrain model, described in Section 2.2, is illustrated in Figure 2. The rotor dynamics are first simulated in OpenFAST, with a simplified drivetrain setup, represented by a spring-damper system with only a torsional degree of freedom. The equivalent drive-shaft torsional spring and damping constant are given in Table 2. The tower top position ($\vec{X}$), low speed shaft (LSS) force, LSS moment ($\vec{F}, \vec{M}$), and generator speed are used as input to the SIMPACK drivetrain setup. A proportional-integral (PI) controller is used to couple the input generator speed (ω_{Gen}) from OpenFAST and the resulting generator speed in SIMPACK due to applied loads and tower top motion. This is to maintain the same dynamic condition between the two independent models.

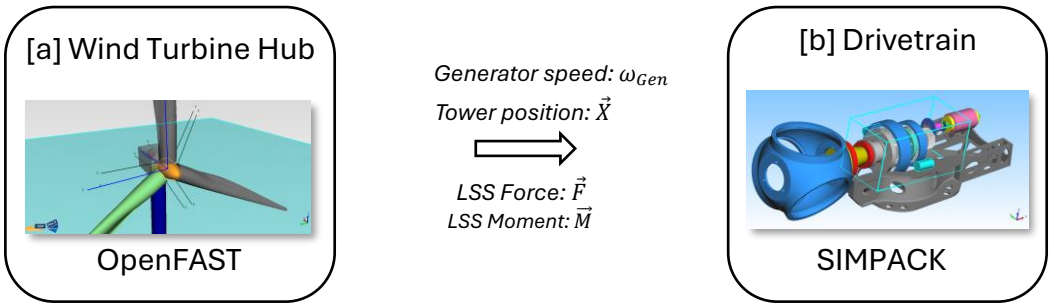

Figure 2. Flow of information between the two models in the decoupled approach.

2.4 Blade damage model

Khoshmanesh et al. [6] conducted a fatigue tension test on a spar-to-shear web assembly representative of a wind turbine blade. During the initial damage phase, marked by the appearance of transverse cracks, the stiffness decreased by less than 2%, whereas the damping increased by about 18%. During the crack saturation phase, the average stiffness reduction was 4.7%. The test specimen experienced a total average stiffness reduction of 8.6% before final failure. While this study focused on only a part of the wind turbine (WT) blade cross-section, and its findings may not directly apply to the more complex structure of a full blade, it provides valuable insights into the relationship between blade damage and stiffness reduction.

In this paper, to study the effect of blade damage on the drivetrain system, the blade stiffness in either the flap-wise or edge-wise directions is reduced in a range between 0.1 and 2% from its healthy value. Since structural damping is inherently related to stiffness, it must also be adjusted. The relationship between the modal damping ratio (ζ) and stiffness proportional damping (β) is expressed as follows [12] :

$$\beta_j = {}^{\zeta_j}/_{\pi\omega_j} \quad (1)$$

where, j is the j^{th} mode ($j\epsilon\{1,2,3\}$), corresponding to the first two flap-wise bending modes and first edge-wise bending mode; β is the stiffness proportional damping (Rayleigh damping) co-efficient, ζ_j is the modal damping ratio for the j^{th} mode, and ω_j is the natural frequency of the j^{th} mode given by

$$\omega_j = (1/2\pi)\sqrt{K_{jj}/M_{jj}} \quad (2)$$

with K_{jj} and M_{jj} represent the stiffness and mass terms for the j^{th} mode, respectively. Using Eq. (1), the effect of local stiffness changes can be incorporated into the modal damping ratio, as follows:

Step 1: Derive initial β_j

Use Eq. (1) to calculate intial β_j using the original modal damping (ζ_j) and natural frequency (ω_j) associated with the healthy blade stiffness distribution (EI)

Step 2: Modify stiffness distribution $E'I'$ and compute new natural frequency (ω_j')

Apply stiffness reduction at the selected blade location and use a Finite Element (FE) solver, e.g. BModes [13], to obtain the modified natural frequency (ω_j')

Step 3: Calculate New Modal Damping Ratio (ζ_j')

Use Equation (1) to calculate the new modal damping ζ_j' with the updated natural frequency (ω_j') from step 2, while keeping β_j constant.

Step 4: Run Aeroelastic Simulations

Incorporate modified damping ratio (ζ_j') for each mode ($j\epsilon\{1,2,3\}$) and stiffness distribution ($E'I'$), into OpenFAST simulations.

Following the above procedure ensures that the contribution of local stiffness changes to the global modal damping is accurately captured, as shown in Figure 3. The blade damage conditions investigated include various local stiffness reduction levels, with changes in flap or edge-wise stiffness of -0.1%, -0.5%, -1.0%, and -2.0%. Each case considers a 1.0 m damage length at nine locations along the blade, ranging from 5 m to 85 m from the root, with a 10 m interval between locations. This sums up to a total of 504 simulations. For each damage case, a separate damping ratio is calculated based on the steps outlined above. Figure 4 shows the change in modal damping ratio of the 1st and 2nd flap-wise modes due to a stiffness reduction of 0.1 to 2% at 45 m from the blade root. It can be seen from Figure 4 that the modal damping ratio (ζ) reduces with stiffness reduction, which is a consequence of the proportional damping model.

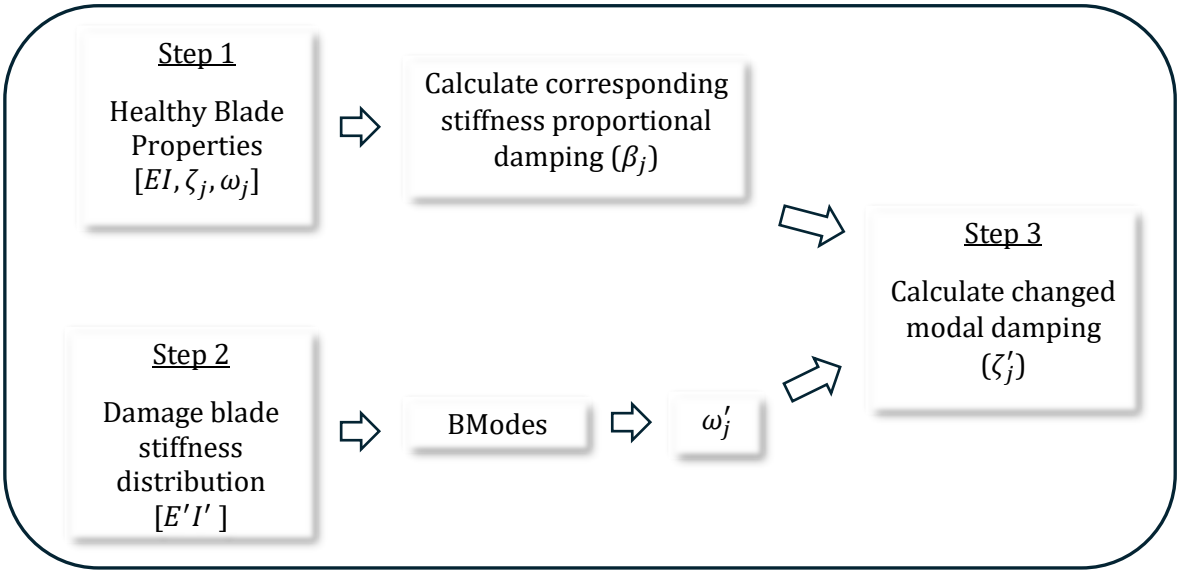

Figure 3. Procedure for including stiffness reduction into the modal damping ratio calculation

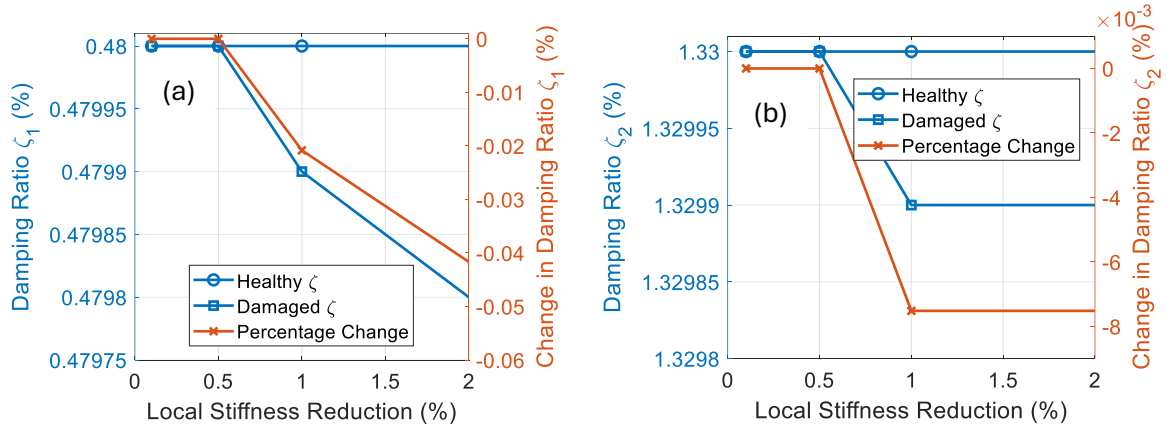

Figure 4. Modal damping ratio change with flap-wise stiffness reduction from 0.1 to 2% at 45 m location from blade root (a) 1st flap mode (b) 2nd flap mode.

2.5 Signal processing

All the blade damage cases listed in section 2.4 were simulated for 3000 s with a signal sampling frequency (f_s) of 400 Hz, discarding the initial 1500 s to avoid initial transient effects. The remaining signals were divided into five segments with 50% overlap and each window was anlaysed in the frequency domain. The analysis procedure involves the following steps :

1) A Discrete Fourier Transform (DFT) is applied to the windowed signal (x_n). The DFT is defined as,

$$X_k = \sum_{n=1}^{N} x_n e^{-2\pi i \frac{k}{N} n} \quad (3)$$

Where $k \in [0, N-1]$ is the frequency index.

2) To mitigate energy leakage, the Hanning window function (w_n) is applied to the sampled signal x_n to obtain the PSD:

$$S_{xx}(k) = \frac{2X_k \bar{X}_k}{W f_s} \quad (4)$$

Where $W = \sum_{n=1}^{N} w_n$ and $\bar{X}_k$ is the complex conjugate of X_k.

3) The Root Mean Square (RMS) of the 1P frequency with a $\pm 0.02\ Hz$ bandwidth is calculated as:

$$RMS = \sqrt{\sum_k S_{xx}(k) . \frac{f_s}{N}} \quad (5)$$

Taking the RMS value within a certain bandwidth ensures that fluctuations in 1P-related energy are captured robustly, providing a more stable indication of damage progression compared to tracking only the peak amplitude.

3. Results and discussion

The proposed sensitivity analysis is divided into two parts. The first sub-section focuses on the system dynamic response from the rotor side, followed by the analysis of the drivetrain system responses in the second sub-section.

3.1 Rotor dynamics

Figure 5 shows the absolute differences in the 1P RMS of LSS shear force in the side-side direction (F_{ys}), between healthy and damaged conditions across different blade spans and wind speeds. Figures 5 (a) and (b) refer to flap-wise and edge-wise stiffness reduction cases, respectively. LSS F_{ys} is the input force to the drivetrain setup and is measured relative to the fixed reference frame. Figure 5 includes a total of nine bar groups, corresponding to nine locations from the blade root to the tip. Each bar group represents seven wind speeds, from 8 to 25 m/s, listed in increasing order. The magnitudes corresponding to different damage levels (0.1-2% stiffness change) are stacked on top of each other for each wind speed within a given blade location. A comparison between Figure 5 (a) and (b) reveals that the 1P harmonic of LSS F_{ys} exhibits the highest sensitivity to flap-wise stiffness reduction at around the blade mid-span (~45 m) and at the rated wind speed of 11.4 m/s for same amount of stiffness change. This could be due to the mid-span of the blade being more susceptible to maximum bending stresses.

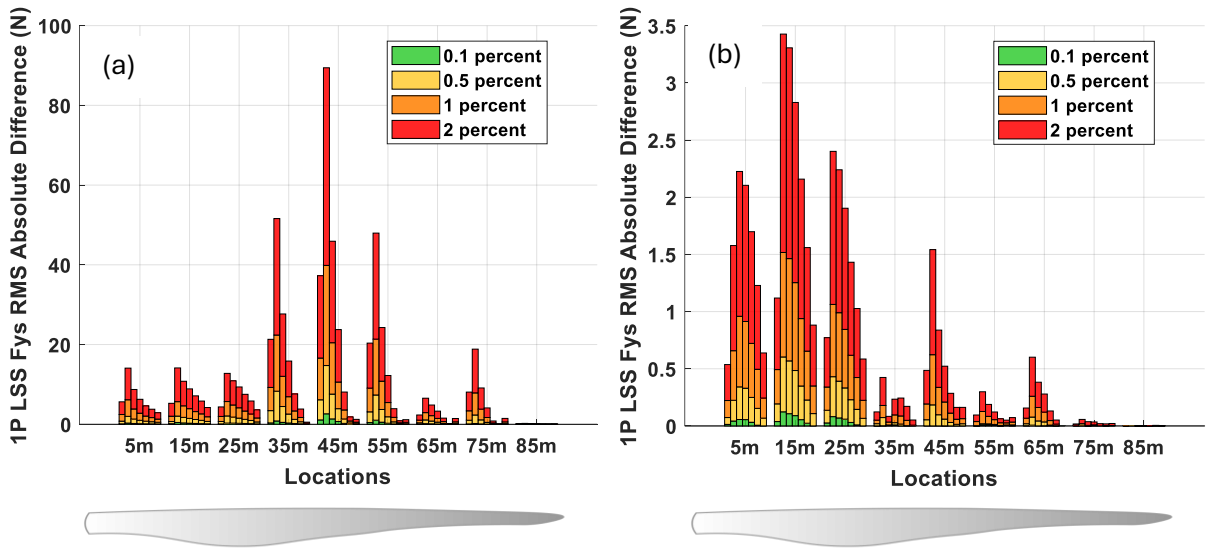

Figure 5. Difference in 1P LSS F_{ys} RMS between healthy and damage conditions due to change in blade (a) flap-wise (b) edge-wise stiffness at different span from root for the wind speeds 8, 11.4, 13, 15, 18, 21, 25 m/s.

While a 2% stiffness change contributes to around 50 N change in the 1P RMS of LSS F_{ys} in the flap-wise direction at ~45 m and rated wind conditions (Figure 5 (a)), it only contributes to a 1.9 N increase in the edge-wise direction at ~ 15m and rated wind conditions, (Figure 5 (b)). From Figure 5 (a), it is also evident that a 0.1% reduction in flap-wise stiffness alters the 1P RMS by only 2.6 N at ~45 m and rated wind conditions.

From both subplots, it can be concluded that blade damage associated with flap-wise or edge-wise stiffness reduction near the blade tip contributes significantly less to the change of 1P RMS. Therefore, in this case, in the absence of additional information, it may be challenging to distinguish damage at the blade tip based only on the value of 1P RMS. A similar conclusion applies to damage near the blade root (Figure 5 (a-b)).

3.2 Drivetrain response analysis

In Figure 6, the 1P RMS values are plotted for the gearbox housing side-side velocity, upwind main bearing (INP_A: Input A) and rear bearing (INP_B: Input B) side-side velocity, all due to flap-wise stiffness changes at 45 m from the blade root. It can be observed in all the subplots that the damage progression from 0.1% to 2% is distinctly visible around rated wind speed (11.4, 13, and 15 m/s). The damage progression trends near the cut-in (8 m/s) and cut-out wind speeds (21 and 25 m/s) are less pronounced. This may be attributed to the fact that the 1P change in LSS F_{ys} at those wind speeds shows a significantly lower contribution compared to the rated wind speed (Figure 5 (a)). It is also noticeable that out of all these subplots housing velocity seems more sensitive to damage progression.

In Figure 7, the correlations between the LSS F_{ys} and upwind main bearing and rear bearing side-side 1P RMS velocities are presented for flap-wise stiffness reduction at 45 m from the blade root. The figure shows how the local damage in a wind turbine blade is translated into system responses observed in different drivetrain components.

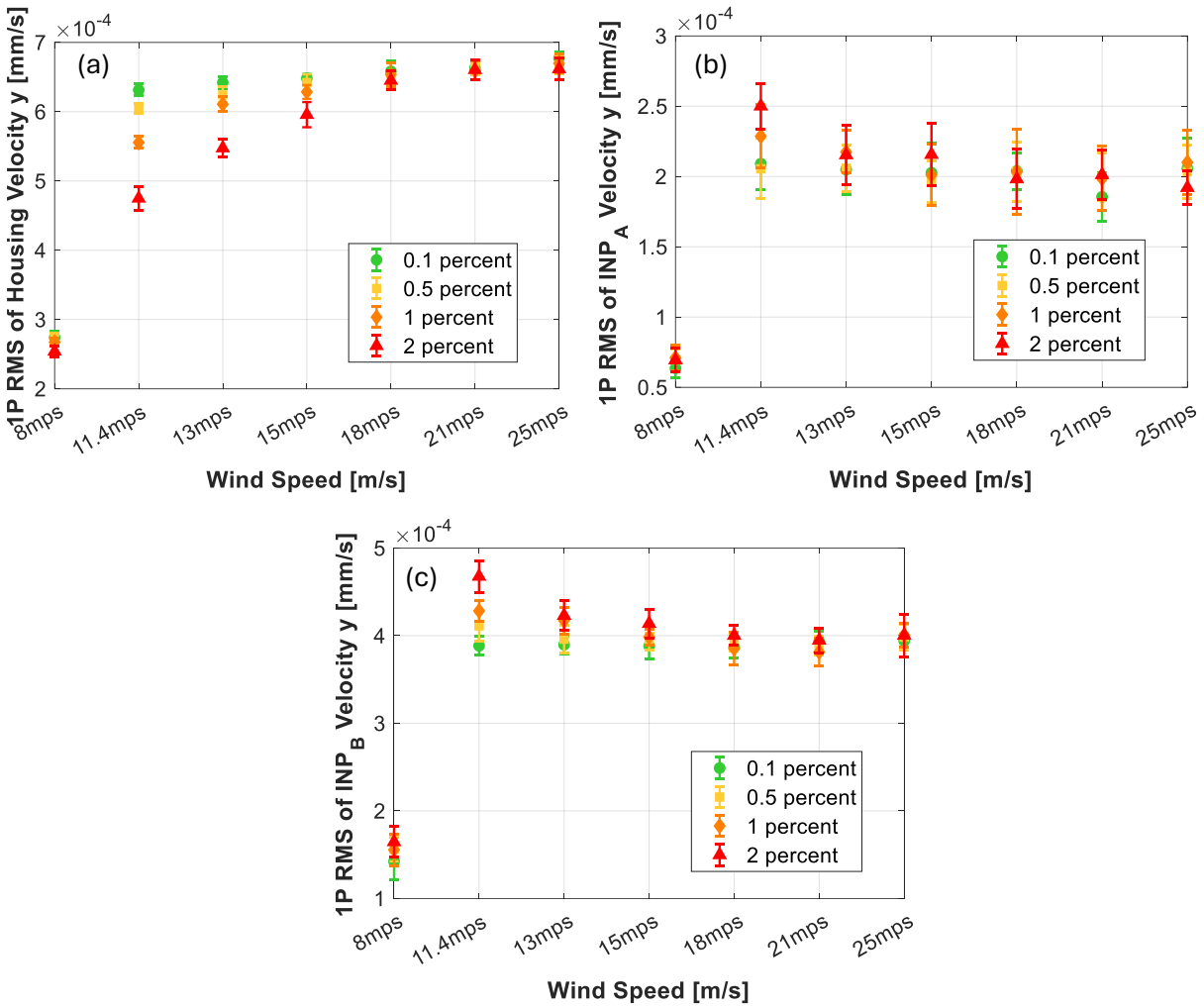

Figure 6. 1P RMS values for (a) gearbox housing side-side velocity, (b) upwind front bearing (INP_A), (c) upwind rear bearing (INP_B) side-side velocity at different wind speeds due to blade flap-wise stiffness changes at 45m from blade root.

From Figure 7, it can be observed that at most wind speeds (especially around rated), the drivetrain responses increase slightly with LSS F_{ys}, showing clear damage progression due to flap-wise stiffness reduction (0.1 to 2%) at the 45 m blade span. While the induced damage causes a change in the shear force and 1P RMS velocities, the magnitude of this change is relatively small and would likely be difficult to detect on a real operating turbine [14].

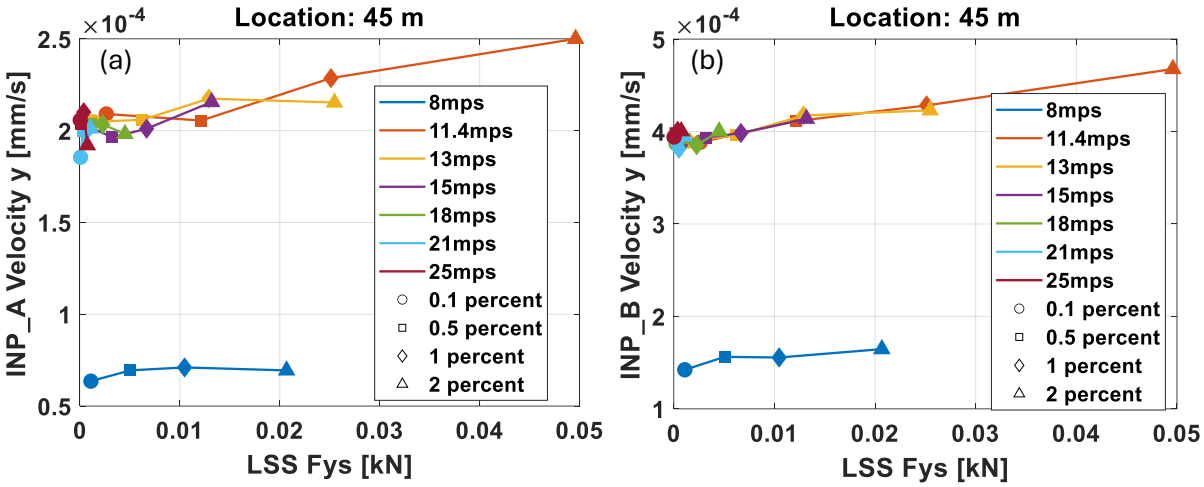

Figure 7. Correlations between the LSS F_{ys} and (a) upwind main bearing (INP_A) side-side velocity (b) rear bearing (INP_B) side-side 1P RMS velocities, due to different stages of the flap-wise stiffness reduction at 45 m from blade root.

4. Conclusions

In this paper, the effect of local stiffness reduction in wind turbine blades on drivetrain CMS signals was studied for the DTU 10MW reference wind turbine. A decoupled approach, combining an aeroelastic solver and an independent drivetrain model, was adopted to achieve the proposed goal. Only changes in the 1P RMS values caused by the introduction of the blade damage were considered in this study, serving as an initial step in the investigation. First, the impact of blade local stiffness change on the rotor dynamics was investigated by analysing the 1P peak amplitudes of the LSS side-side shear force. The results showed that, compared to the blade tip and root regions, the mid-span region is the most sensitive to the same amount of damage. The maximum change in the 1P RMS values occurred near the rated wind speed (11.4, 13, 15 m/s).

Thereafter, the simulated LSS shear forces, moments, and tower top position vector were transferred to the independent drivetrain setup in the SIMPACK multibody-dynamics platform. The 1P RMS of gearbox housing, main and rear bearing side-side velocities for both healthy and damaged conditions were analysed. Similar to the LSS side-side shear force, the drivetrain responses exhibited clear damage progression at the rated wind speed. However, for the wind speeds close to the cut -in and cut-out regions, the damage progression trend was unclear. Considering the magnitude of the associated error bars, a longer simulation time might be required for more clarity. Finally, the correlation between the LSS side-side shear force and the front and rear bearing side-side velocities at the blade mid-span (~45 m location) demonstrated a clear progression of damage as the stiffness reduction increased from 0.1% to 2.0%. Future studies should investigate the impact of higher local blade stiffness reduction and the inclusion of turbulence on drivetrain CMS signal sensitivity. Such work will be used to determine at what level of stiffness change (and thus damage) the changes to system response become significant and could be used in a practical condition monitoring system.

References

[1] D. Zappalá and P. J. Tavner, 'Wind Turbine Reliability - Maintenance Strategies', in *Comprehensive Renewable Energy*, Elsevier, 2022, pp. 353–370. doi: 10.1016/B978-0-12-819727-1.00154-0.
[2] M. A. Fremmelev, P. Ladpli, E. Orlowitz, N. Dervilis, M. McGugan, and K. Branner, 'A full-scale wind turbine blade monitoring campaign: detection of damage initiation and progression using medium-frequency active vibrations', *Structural Health Monitoring*, vol. 22, no. 6, pp. 4171–4193, Nov. 2023, doi: 10.1177/14759217231163471.
[3] T. Varouxis, V. K. Dertimanis, I. Abdallah, E. Chatzi, V. Pakrashi, and A. Malekjafarian, 'Deep-Learning-based damage detection of an experimentally tested full-scale wind turbine blade.', *eJNDT*, vol. 29, no. 7, Jul. 2024, doi: 10.58286/29852.
[4] K. Kong, K. Dyer, C. Payne, I. Hamerton, and P. M. Weaver, 'Progress and Trends in Damage Detection Methods, Maintenance, and Data-driven Monitoring of Wind Turbine Blades – A Review', *Renewable Energy Focus*, vol. 44, pp. 390–412, Mar. 2023, doi: 10.1016/j.ref.2022.08.005.
[5] Y. Zhang, F. Avallone, and S. Watson, 'Wind turbine blade trailing edge crack detection based on airfoil aerodynamic noise: An experimental study', *Applied Acoustics*, vol. 191, p. 108668, Mar. 2022, doi: 10.1016/j.apacoust.2022.108668.
[6] S. Khoshmanesh, S. J. Watson, and D. Zarouchas, 'The effect of the fatigue damage accumulation process on the damping and stiffness properties of adhesively bonded composite structures', *Composite Structures*, vol. 287, p. 115328, May 2022, doi: 10.1016/j.compstruct.2022.115328.
[7] National Renewable Energy Laboratory, 'OpenFAST Documentation - Release v2..3.0', Oct. 2020.
[8] J. Jonkman, 'AeroDyn v15 User's Guide and Theory Manual'. [Online]. Available: https://www.nrel.gov/wind/nwtc/assets/pdfs/aerodyn-manual.pdf
[9] N. J. Abbas, D. S. Zalkind, L. Pao, and A. Wright, 'A reference open-source controller for fixed and floating offshore wind turbines', *Wind Energ. Sci.*, vol. 7, no. 1, pp. 53–73, Jan. 2022, doi: 10.5194/wes-7-53-2022.
[10] C. Bak *et al.*, 'Light Rotor: The 10-MW reference wind turbine', Jan. 2012.
[11] S. Wang, A. R. Nejad, and T. Moan, 'On Initial Design and Modelling of a 10 MW Medium Speed Drivetrain for Offshore Wind Turbines', *J. Phys.: Conf. Ser.*, vol. 1356, no. 1, p. 012024, Oct. 2019, doi: 10.1088/1742-6596/1356/1/012024.
[12] M. Liu and D. G. Corman, 'Formulation of Rayleigh damping and its extensions', *Computers & Structures*, vol. 57, no. 2, pp. 277–285, 1995.
[13] NREL, 'BModes'. [Online]. Available: https://www.nrel.gov/wind/nwtc/bmodes.html
[14] ISO 10816-21, 'Mechanical vibration - Evaluation of machine vibration by measurements on non-rotating parts - Part 21: Horizontal axis wind turbines with gearbox'. 2015.